

Article

Experimental Investigations on the Electrical Conductivity and Complex Dielectric Permittivity of $Zn_xMn_{1-x}Fe_2O_4$ ($x = 0$ and 0.4) Ferrites in a Low-Frequency Field

Iosif Malaescu^{1,2} , Paula Sfirloaga^{3,4} , Catalin N. Marin^{1,*}, Madalin O. Bunoiu¹  and Paulina Vlazan³

¹ Faculty of Physics, West University of Timisoara, Bd. V. Parvan No. 4, 300223 Timisoara, Romania; iosif.malaescu@e-uvvt.ro (I.M.); madalin.bunoiu@e-uvvt.ro (M.O.B.)

² Institute for Advanced Environmental Research, West University of Timisoara (ICAM-WUT), Oituz Str., No. 4, 300086 Timisoara, Romania

³ National Institute of Research and Development for Electrochemistry and Condensed Matter, 144 Dr. A. P. Podeanu, 300569 Timisoara, Romania; paulasfirloaga@gmail.com (P.S.); vlazanp@yahoo.com (P.V.)

⁴ Spin-Off Nattive-Senz SRL, Str. Dr. A. P. Podeanu, Nr. 144, 300569 Timisoara, Romania

* Correspondence: catalin.marin@e-uvvt.ro

Abstract: Two samples of $Zn_xMn_{1-x}Fe_2O_4$ ($x = 0$, sample A; and $x = 0.4$, sample B) were synthesized by the hydrothermal method. From complex impedance measurements in the range 100 Hz–2 MHz and for temperatures T between 30 and 130 °C, the barrier energy between localized states ΔE_{relax} was determined for the first time in these samples. For sample B, a single value of ΔE_{relax} was highlighted (0.221 eV), whilst, for sample A, two values were obtained (0.012 eV and 0.283 eV, below 85 °C and above 85 °C, respectively), associated with two zones of different conductivities. Using the Mott's VRH model and the CBH model, we determined for the first time both the bandgap energy barrier (W_m) and the hopping (crossover) frequency (ω_h), at various temperatures. The results show that, for sample A, W_m has a maximum equal to 0.72 eV at a temperature between 70 and 80 °C, whilst, for sample B, W_m has a minimum equal to 0.28 eV at a temperature of 60 °C, the results being in good agreement with the temperature dependence of the static conductivity $\sigma_{DC}(T)$ of the samples. By evaluating σ_{DC} and eliminating the conduction losses, we identified, using a novel approach, a dielectric relaxation phenomenon in the samples, characterized by the activation energy $E_{A,rel}$. At various temperatures, we determined $E_{A,rel}$, which ranged from 0.195 eV to 0.77 eV. These results are important, as understanding these electrical properties is crucial to various applications, especially in technologies where temperature variation is significant.

Keywords: manganese ferrites; Zn-Mn ferrite; complex impedance measurements; electrical conductivity; complex dielectric permittivity; VRH and CBH models



Citation: Malaescu, I.; Sfirloaga, P.; Marin, C.N.; Bunoiu, M.O.; Vlazan, P. Experimental Investigations on the Electrical Conductivity and Complex Dielectric Permittivity of $Zn_xMn_{1-x}Fe_2O_4$ ($x = 0$ and 0.4) Ferrites in a Low-Frequency Field. *Crystals* **2024**, *14*, 437. <https://doi.org/10.3390/cryst14050437>

Academic Editors: Raphaël P. Hermann and Haibo Zhang

Received: 15 March 2024

Revised: 29 April 2024

Accepted: 1 May 2024

Published: 4 May 2024

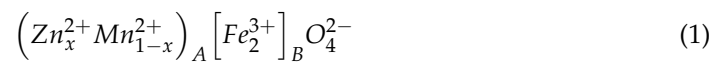


Copyright: © 2024 by the authors. Licensee MDPI, Basel, Switzerland. This article is an open access article distributed under the terms and conditions of the Creative Commons Attribution (CC BY) license (<https://creativecommons.org/licenses/by/4.0/>).

1. Introduction

Ferrites represent an important class of materials, being used in many applications: in the electronic and telecommunication industry [1,2], in the field of biomedical applications, photocatalysis, ferrofluid technology, etc. [3–5]. This wide range of applications is due to their electrical, magnetic, optical, or catalytic properties, which can be obtained by appropriate variations in the particle size, chemical composition, and the processing parameters of the ferrite [6–8]. The general chemical formula of ferrites is of the form $M^{2+}O^{2-}Fe_2^{3+}O_3^{2-}$, where M is a divalent element of the type Mn, Co, Ni, and Mg or a metallic combination of mono, bi, or trivalent elements, which is equivalent to a divalent element. In the reference [9], the authors carried out experimental investigations on the structural transformations in manganese ferrite induced by heat treatment, concluding that, above 400 °C, a chemical phase transformation occurs from spinel $MnFe_2O_4$ to perovskite $MnFeO_3$, which strongly affects both the magnetic and electrical behavior of the samples.

Among the useful ferrites which have been developed, the Mn-Zn ferrite with a cubic spinel structure can be highlighted. The cation distribution in the ferrite structure is described by the following formula:



where the round bracket and the square bracket represent the tetrahedral site (A-site) and the octahedral site (B-site), respectively [10]. The substitution of Mn^{2+} with Zn^{2+} ions in the tetrahedral site will lead to the improvement of the structural, morphological, magnetic, and electrical properties of Mn-Zn ferrite [11–13]. More researchers have obtained significant results regarding the obtaining methods, morpho-structural characterization, and magnetic properties of Mn-Zn compounds [14–16]. There are few articles in the literature regarding the thermo-impedance analysis (dependence on both the temperature and the frequency of the complex impedance and the electrical conductivity) of Mn-Zn ferrites. For this reason, in the present paper, the determination of the electrical conductivity (σ) and the complex dielectric permittivity (ϵ) in the low-frequency field for $Zn_x Mn_{1-x} Fe_2 O_4$ compounds as well as the experimental studies regarding the frequency and temperature dependence of σ and ϵ are very important. Knowledge of the electrical and dielectric properties of these materials, in addition to their magnetic properties, is very useful in applications such as energy storage, photocatalytic applications [17], or microelectronic applications such as power electronics-integrated LC filters [18].

In this context, the experimental measurements of electrical conductivity and complex dielectric permittivity are very useful to obtain information regarding the possibility of using these materials in various applications. Thus, based on thermo-impedance measurements in a frequency range of 20 Hz–2 MHz and at different temperatures T in the range of 30–130 °C, the purpose of this paper is to determine the frequency and temperature dependence of the electrical conductivity $\sigma(f, T)$ and the complex dielectric permittivity $\epsilon(f, T)$ for the prepared ferrites, $Zn_x Mn_{1-x} Fe_2 O_4$ (with $x = 0$ and 0.4), and highlight the possible changes in the conduction regime and the transition temperatures from one regime to another. Also, another purpose of the present paper is to comparatively explain the conduction mechanisms from the samples, using both the obtained results and the VRH (variable range hopping) of Mott [19] and the CBH (correlated barrier hopping) [20] theoretical models, and determine some parameters of these models (the crossover frequency, the activation energy for electrical conduction, and the bandgap energy barrier).

2. Sample Characterization and Experiments

2.1. Synthesis

Using the hydrothermal method [21], two samples were synthesized for the experimental investigations: a manganese ferrite sample ($MnFe_2O_4$) for $x = 0$ (Sample A) and another sample (Sample B), substituted with Zn^{2+} ions ($Zn_{0.4}Mn_{0.6}Fe_2O_4$), for $x = 0.4$.

The reactants used in the technological process of the two samples' preparation were of analytical grade and purchased from Merck. For the preparation of sample A, the following reagents were used: 1.7895 g $Mn(NO_3)_2 \cdot H_2O$ and 4.8372 g $Fe(NO_3)_3 \cdot 2H_2O$. Metal salts were dissolved in distilled water and then 1 M NaOH solution was added until the pH reached a value of 11. The manganese ferrite doped with Zn (sample B) was obtained using the same reactants as in the case of sample A, with the difference that 4% of $Mn(NO_3)_2 \cdot 4H_2O$ was replaced by $Zn(NO_3)_2 \cdot 6H_2O$. As a result, the following quantities of reactants were used in the technological process of sample B: 1.2554 g $Mn(NO_3)_2 \cdot H_2O$, 4.8372 g $Fe(NO_3)_3 \cdot 2H_2O$, and 0.5949 g of $Zn(NO_3)_2 \cdot 6H_2O$ solution with a concentration of 0.002 M. The mixture thus obtained for both sample A and sample B was placed in a Morey-type autoclave and maintained at 220 °C for 12 h. After settling and filtering, the resulting precipitates for sample A and sample B were separately washed with distilled water on filter paper and then dried in an air-oven at 800 °C, thus obtaining $MnFe_2O_4$ -type and $Zn_{0.4}Mn_{0.6}Fe_2O_4$ -type ferrite powders, respectively.

2.2. Characterization Techniques

The phase structure of the prepared samples was investigated by X-ray diffraction (XRD) using the PANalytical-X'Pert PRO MRD diffractometer—Philips, FEI Company PANalytical BV Netherlands, with Cu-K α radiation ($20^\circ \leq 2\theta \leq 80^\circ$). The results were interpreted with the X'PERT PRO MRD software, FullProf software Version: 2.2b (2.2.2), finally obtaining the diffractogram of the material. Fourier-Transform Infrared Spectroscopy (FTIR) spectra were obtained using a Shimadzu Prestige-21 spectrometer, Japan, in the range 400–4000 cm^{-1} . For the identification of the absorption bands, the existing data in the literature were used [22]. The morphology of the samples was investigated with an FEI Inspect S microscope model scanning electron microscopy (SEM), FEI Company PANalytical Netherlands. At the same time, using the EDX facility of the scanning electron microscope, the elemental analysis of the samples was carried out. The magnetic studies were carried out using the inductive method with a hysteresis graph [23] at a low frequency (50 Hz). Based on the complex impedance measurements in the frequency range of 100 Hz–2 MHz and at different temperatures, between 30 and 130 $^\circ\text{C}$, the frequency and temperature dependence of the electrical conductivity and complex dielectric permittivity of the prepared samples were determined, using an LCR meter (Agilent E-4980-A type) USA, in conjunction with a laboratory experimental setup [24], similar to ASTM D150-98 [25].

3. Results and Discussion

3.1. X-ray Diffraction Analysis

The X-ray diffraction patterns of the prepared samples, $\text{Zn}_x\text{Mn}_{1-x}\text{Fe}_2\text{O}_4$ (where $x = 0$ and 0.4), are shown in Figure 1.

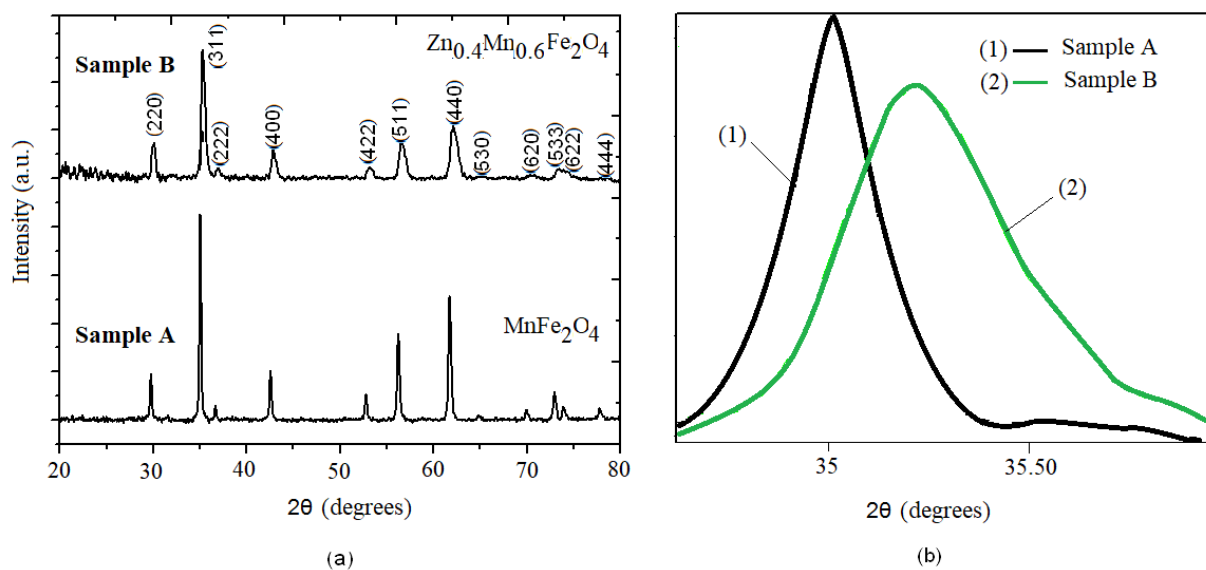


Figure 1. (a) X-ray diffraction patterns of samples A (MnFe_2O_4) and B ($\text{Zn}_{0.4}\text{Mn}_{0.6}\text{Fe}_2\text{O}_4$); and (b) diffraction peak (311) for samples A and B.

The diffraction pattern from Figure 1a shows that both sample A and sample B contain peaks that match the standard data of cubic spinel MnFe_2O_4 (JCPDS Card no. 75-0034). Also, the XRD pattern obtained for both samples shows that the materials are well crystallized, without any secondary phases (Figure 1). The materials crystallized with the cubic spinel type structure, in the $\text{Fd-}3\text{m}$ space group. The average crystallite size and lattice constant for the investigated samples were computed using the Scherrer formula and are listed in Table 1.

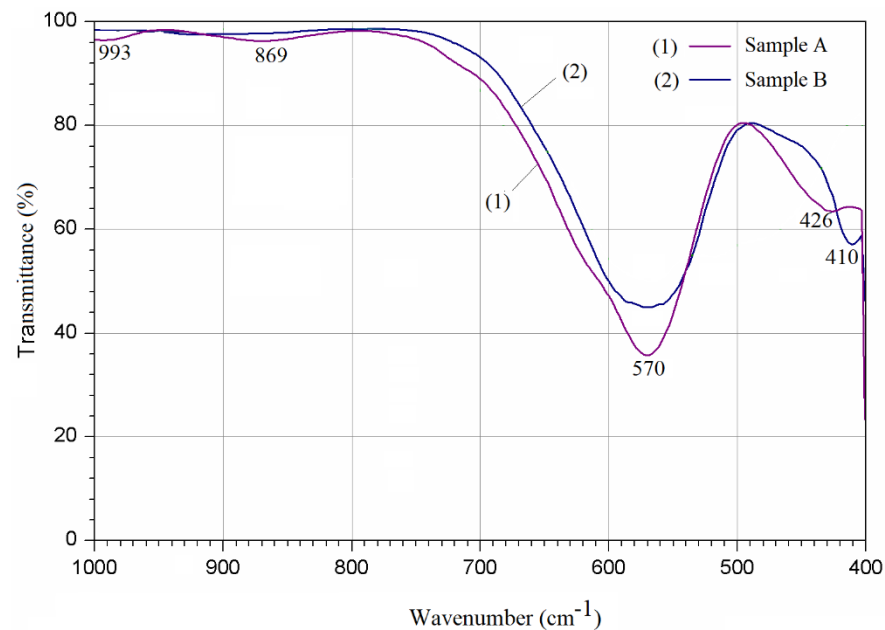
Table 1. Computed values of crystallite size and lattice constant for different Zn concentrations x , corresponding to samples A and B.

Samples	Zn Concentration (x)	Crystallite Size (nm)	Lattice Constant (\AA)
A (MnFe_2O_4)	0	45	8.498(1)
B ($\text{Zn}_{0.4}\text{Mn}_{0.6}\text{Fe}_2\text{O}_4$)	0.4	23.9	8.48(1)

From Table 1, it can be seen that the average size of the crystallites is lower for $x = 0.4$ than for $x = 0$. This may be correlated to the broadening of the diffraction maximum (311) for the Zn-substituted manganese ferrite (sample B), as seen in Figure 1b. At the same time, from Table 1, it can be seen that the lattice constant of sample B substituted with Zn ions ($x = 0.4$) decreases slightly compared to that of sample A, un-substituted ($x = 0$). This result can be correlated with the fact that the ionic radius of Zn^{2+} in the tetrahedral position is 0.060 nm, being slightly smaller than the ionic radius of Mn^{2+} in the tetrahedral position, which is 0.066 nm [26].

3.2. FTIR Analysis

The FTIR spectra of the prepared samples A and B are shown in Figure 2.

**Figure 2.** FTIR spectra for $\text{Zn}_x\text{Mn}_{1-x}\text{Fe}_2\text{O}_4$ ferrite samples, with $x = 0$ (sample A) and $x = 0.4$ (sample B).

From Figure 2, it can be seen that the FTIR absorption spectrum of sample A (MnFe_2O_4) shows a main absorption band ν_1 centered around the value of 570 cm^{-1} , attributed to the stretching vibrations of the tetrahedral group, and a second absorption band ν_2 centered around the value of 426 cm^{-1} , attributed to the octahedral group [27]. The two absorption bands indicate the formation of the metal–oxygen bond (M–O) both in the tetrahedral $(\text{M–O})_A$ and octahedral $(\text{M–O})_B$ sites in the spinel structure, confirming the result obtained by X-ray diffraction for these samples (Figure 1), in which only one phase appears. From Figure 2, it can also be observed that, for the zinc concentration $x = 0.4$ in the MnFe_2O_4 structure (sample B), the spectrum shows the two characteristic absorption bands but with a decrease in the main absorption band, thus indicating the formation of the spinel phase [28].

3.3. Scanning Electron Microscopy

The SEM images and the result of the EDX elemental analysis of the synthesized materials, $Zn_xMn_{1-x}Fe_2O_4$ (with $x = 0$ and 0.4), are shown in Figure 3.

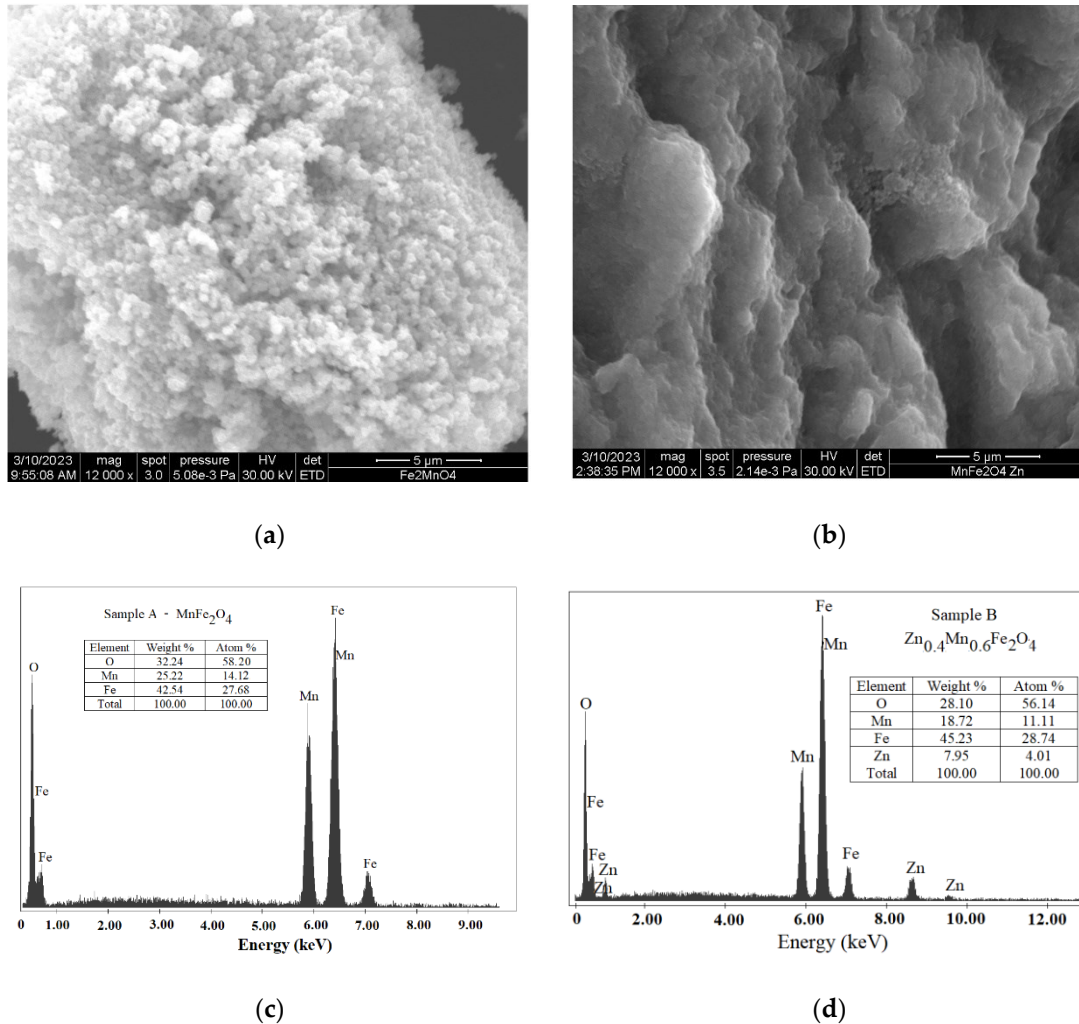


Figure 3. SEM images for samples A (a) and B (b) and EDX elemental analysis for samples A (c) and B (d).

From Figure 3a,b, one can observe the existence of agglomerated particles of various sizes in the synthesized samples and an increase in agglomeration in the case of manganese ferrites doped with Zn. On the other hand, as shown in Figure 3c,d, the results of EDX (which is a semi-quantitative analysis) confirm the presence of Fe, Mn, Zn, and O elements in the samples, as well as the phase purity of the obtained materials.

3.4. Magnetic Properties

Figure 4 shows the specific magnetization curves of the prepared $Zn_xMn_{1-x}Fe_2O_4$ (with $x = 0$ and 0.4) ferrite samples. The curve in Figure 4a, corresponding to manganese ferrite sample A, $MnFe_2O_4$ (with $x = 0$), reveals a narrow hysteresis behavior, thus indicating the soft ferrimagnetic nature of the material. The curves in Figure 4b, corresponding to sample B, $Zn_{0.4}Mn_{0.6}Fe_2O_4$ (with $x = 0.4$), show that, by introducing Zn into manganese ferrite, the variation in magnetization with the applied magnetic field has the typical characteristics of a superparamagnetic behavior, such as the absence of hysteresis, coercivity, and zero remanence, as other authors also obtained [26,29,30] for samples of the same kind.

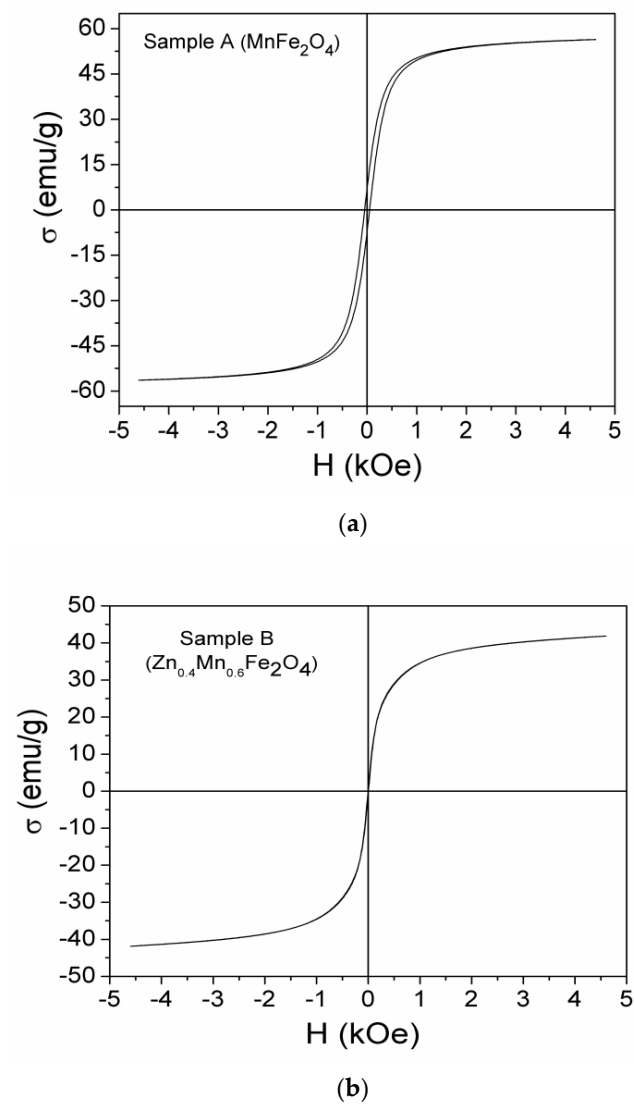


Figure 4. Hysteresis curves of the $\text{Zn}_x\text{Mn}_{1-x}\text{Fe}_2\text{O}_4$ investigated samples: (a) sample A ($x = 0$) and (b) sample B ($x = 0.4$).

Using the magnetic measurements from Figure 4, the following magnetic parameters of the samples were determined: saturation magnetization (σ_s), coercive field (H_c), remanent magnetization (σ_r), and the corresponding remnant ratio (σ_r/σ_s). The obtained values are listed in Table 2.

Table 2. Values of the magnetic parameters for the $\text{Zn}_x\text{Mn}_{1-x}\text{Fe}_2\text{O}_4$ ($x = 0$ and 0.4) ferrite samples.

Sample	σ_s [emu/g]	H_c [kOe]	σ_r [emu/g]	σ_r/σ_s
A (MnFe_2O_4)	58.76	0.049	7.13	0.121
B ($\text{Zn}_{0.4}\text{Mn}_{0.6}\text{Fe}_2\text{O}_4$)	44.21	-	-	-

From Table 2, it can be observed that the saturation magnetization of sample A of manganese ferrite is 58.76 emu/g, being lower than that of bulk manganese ferrite (80 emu/g) [31]. Also, the low value of the remnant ratio σ_r/σ_s of the sample A (see Table 2) represents an indication of the ease with which the magnetization direction reorients towards the direction of the easy-magnetization axis after the removal of the magnetic field, which shows the materials which can be used in biomedical applications or as absorbent materials [32]. At the same time, from Table 2, it can be observed that the saturation magnetization of sample B ($\text{Zn}_{0.4}\text{Mn}_{0.6}\text{Fe}_2\text{O}_4$), having a superparamagnetic behavior, is

44.21 emu/g. The explanation of the decrease in the σ_s value of sample B by doping MnFe_2O_4 ferrite with Zn^{2+} ions can be attributed to the decrease in size of the particles due to the cationic stoichiometry and the occupation of specific sites by ions [33,34].

3.5. Electrical and Dielectric Properties

3.5.1. Complex Impedance

The complex impedance Z is given by the following equation:

$$Z = Z' - iZ'' \quad (2)$$

where Z' and Z'' are the real and imaginary parts of the complex impedance. Figure 5a–d show the frequency dependence of the Z' and Z'' components in the range 0.1 kHz–2 MHz at different temperatures, between 30 and 130 °C, for the investigated samples.

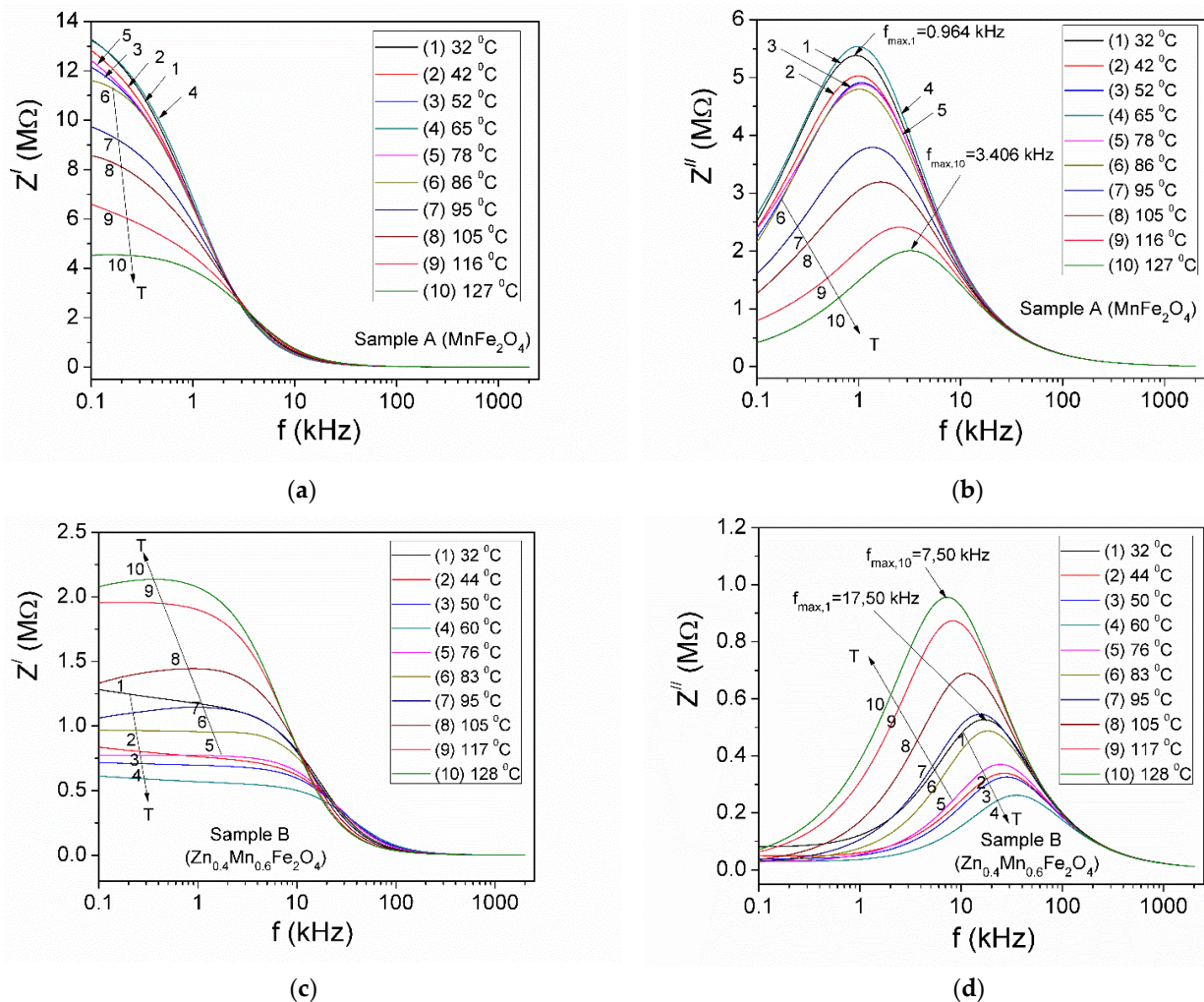


Figure 5. Frequency dependence of the Z' and Z'' components of the complex impedance at different temperatures for (a,b) sample A of MnFe_2O_4 and (c,d) sample B of $\text{Zn}_{0.4}\text{Mn}_{0.6}\text{Fe}_2\text{O}_4$.

As it can be seen from Figure 5, the amplitude of the Z' component decreases with increasing temperature for sample A of manganese ferrite throughout the temperature range (Figure 5a), while, for sample B of Mn-Zn ferrite, the amplitude of Z' decreases with temperature, up to approximately 78 °C (Figure 5c), after which Z' increases by increasing the temperature to 128 °C. Also, it is noted that, at a constant temperature T , the real part Z' of the impedance for sample A (Figure 5a) decreases rapidly up to the frequency $f = 4$ kHz and then decreases slowly with the increase in frequency to $f = 100$ kHz. For sample B

(Figure 5c), at a constant temperature T , the Z' component remains approximately constant up to a frequency of approximately 3 kHz, after which it decreases rapidly with increasing frequency up to 20 kHz and then decreases slowly with the increase in frequency up to $f = 100$ kHz. Next, above 100 kHz, for both samples, in the third region, between 100 kHz and 2 MHz), the Z' components overlap for all the temperatures. Such an evolution with the temperature of the real component Z' shows the semiconductor behavior of sample A over the entire temperature range and up to approximately 78 °C for sample B [35]. This result is in accordance with the structural studies obtained by Hajlaoui et al. [36], which show that increasing the temperature induces the hopping of Fe^{2+} ions towards the tetrahedral sites, where the reduction in Zn ions takes place. As a result, there is a decrease in the electron hopping barrier's height by increasing the temperature, which causes an increase in the electrical conductivity and, therefore, a decrease in the real component Z' of the complex impedance, as was also obtained experimentally.

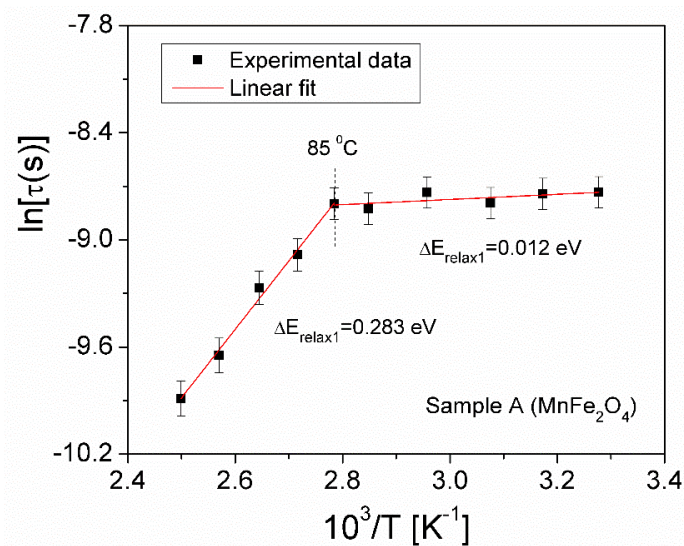
From Figure 5, it can be seen that the amplitude of the Z'' component of the complex impedance decreases with increasing temperature for sample A throughout the temperature range (Figure 5b). For sample B, the amplitude of Z'' decreases with temperature, up to approximately 60–70 °C (Figure 5d), after which Z'' increases by increasing the temperature to 128 °C. Also, the Z'' component presents a maximum at a frequency f_{max} for all the samples and at all the investigated temperatures. For sample A of manganese ferrite, MnFe_2O_4 , the f_{max} frequency moves to lower values by increasing the temperature. In the case of sample B of Mn-Zn ferrite, $\text{Zn}_{0.4}\text{Mn}_{0.6}\text{Fe}_2\text{O}_4$, f_{max} moves towards lower values when the temperature increases up to 60 °C, after which, as the temperature continues to increase up to 128 °C, f_{max} moves towards higher values. This behavior of Z'' shows the existence of an electrical relaxation process [37], which is due to the presence of charge carriers in the investigated samples [19,20], being determined by the hopping of these charge carriers between localized states, in compliance with the VRH of the Mott and Davis model [19]. On the other hand, from Figure 5b,d, it can be seen that the relaxation processes take place at frequencies between 7 kHz and 30 kHz for sample B, while, in the case of sample A, relaxation processes are present at lower frequencies, located in the range 1–4 kHz. This experimental result can be correlated with the fact that, by introducing Zn ions into the manganese sample, there is a decrease in the characteristic time of the hopping of charge carriers over the energy barrier.

Taking into account the values obtained for f_{max} from Figure 5b,d, we determined the relaxation times (τ) corresponding to each temperature T for the two investigated samples using the Debye equation, $2\pi f_{max}\tau = 1$ [38]. Considering that the relaxation time τ depends in an inversely proportional way on the f_{max} frequency, the results show that, in the case of sample A (manganese ferrite MnFe_2O_4), the relaxation time decreases with temperature both at the beginning of the interval between 32 and 65 °C and at raised temperatures between 86 and 127 °C (see Figure 5b). In the case of sample B (manganese ferrite doped with Zn ions), the decrease in relaxation time occurs only at the beginning of the temperature range between 32 and 70 °C, after which an increase in τ with temperature is observed (see Figure 5d). The decrease in the relaxation time in the mentioned temperature ranges, specific to the semiconductor-type behavior of the samples, is in agreement with an Arrhenius-type law:

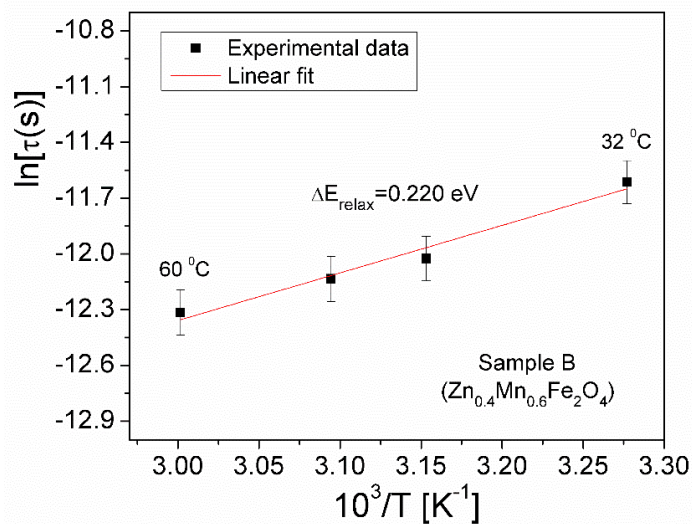
$$\tau = \tau_0 \exp\left(\frac{\Delta E_{relax}}{kT}\right) \quad (3)$$

where k is the Boltzmann constant; τ_0 represents the pre-exponential factor of the relaxation time; and ΔE_{relax} is the activation energy or the barrier energy between the localized states [39]. Figure 6a,b present the plot of dependence $\ln(\tau)$ on $(1000/T)$ for both samples. The measurement error of $\ln(\tau)$ is approximately 0.8%, and it is represented in Figure 6a,b with error bars. The linear fit of the curve from Figure 6a corresponding to sample A (MnFe_2O_4) gives two different slopes, corresponding to the two temperature ranges (below 85 °C and above 85 °C), and the fit of the curve from Figure 6b corresponding to sample B ($\text{Zn}_{0.4}\text{Mn}_{0.6}\text{Fe}_2\text{O}_4$) gives one slope. The curves from Figure 6a,b are fitted with a straight

line with equation $y = a + bx$, where a is the intercept, and b is the slope of the line. For sample A, the fitting parameters are the following: intercept $a = -9.20718$ and slope $b = 144.31527$ (for the temperature range below $85\text{ }^{\circ}\text{C}$) and intercept $a = -19.46419$ and slope $b = 3831.96782$ (for the temperature range above $85\text{ }^{\circ}\text{C}$). For sample B, the fitting parameters are the following: intercept $a = -20.07357$ and slope $b = 2571.78693$. Therefore, for sample A, two activation energy values (0.012 eV and 0.283 eV) associated with two areas of different conductivities are obtained, and, for sample B, a value equal to 0.221 eV is obtained. Similar values in terms of the activation energy have also been obtained by other authors for the same type of ferrites [29,40]. Materials similar to sample A, which have two different conduction regimes (with two different thermal activation energies of conduction), can be used in the creation of sensors in which temperature change is involved.



(a)



(b)

Figure 6. The $\ln(\tau)(T^{-1})$ plots for $\text{Zn}_x\text{Mn}_{1-x}\text{Fe}_2\text{O}_4$ ferrites: (a) sample A ($x = 0$) and (b) sample B ($x = 0.4$).

3.5.2. Electrical Conductivity

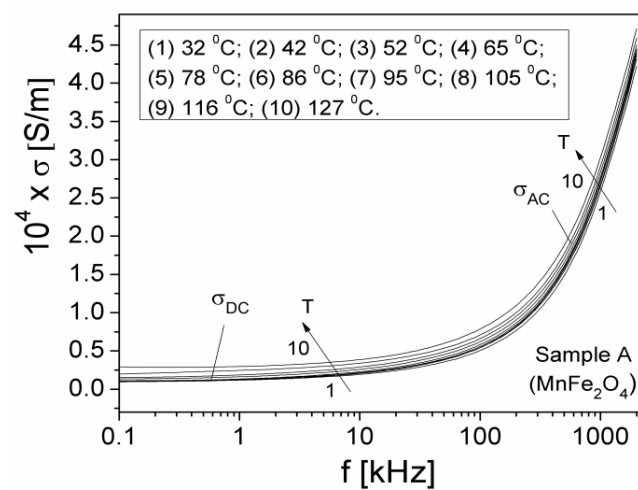
The investigated sample was inserted into a glass cylindrical tube having a diameter $D = 3.8\text{ mm}$ and, therefore, a cross section area $A = 11.34\text{ mm}^2$. The sample in the glass

tube had a thickness of $d = 4$ mm and was in contact with two electrodes, which allowed its connection to the LCR meter [24,25]. At the same time, the glass tube with the sample was placed in an electric oven, thermally insulated and heated by an electric resistance connected to a voltage source, with the temperature T being measured with a thermocouple. The real Z' and imaginary Z'' components of the complex impedance were measured, for each temperature T .

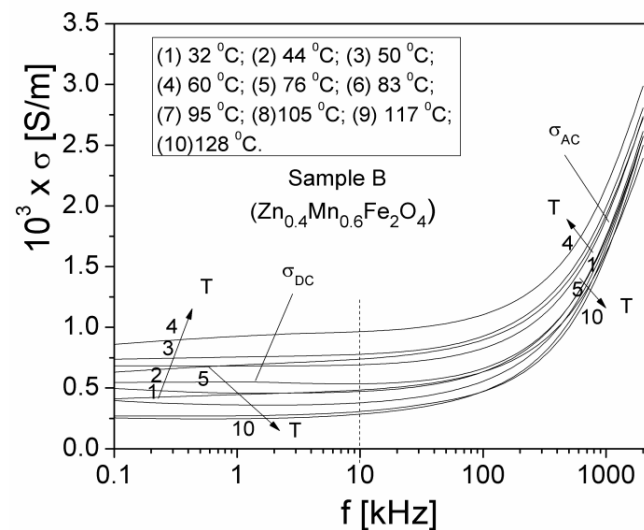
The electrical conductivity can be determined from the measurements of the Z' and Z'' components of complex impedance (Figure 5), using the following equation:

$$\sigma = \frac{Z'}{Z'^2 + Z''^2} \left(\frac{d}{A} \right) \quad (4)$$

In Figure 7, the frequency and temperature dependencies of the conductivity σ of the samples in the 100 Hz to 2 MHz range and at different temperatures between 30 °C and 130 °C are shown.



(a)



(b)

Figure 7. The frequency dependence at different temperatures of the (Z') and (Z'') components of the complex impedance of the $\text{Zn}_x\text{Mn}_{1-x}\text{Fe}_2\text{O}_4$ samples: (a) $x = 0$ and (b) $x = 0.4$.

From Figure 7, it can be seen that, in the case of both samples, for each temperature T , the conductivity σ remains constant at a low frequency, until it nears the frequency of 10 kHz, at which point it increases sharply with increasing frequencies, being in agreement with Jonscher's universal law [41]. The conductivity spectrum $\sigma(f, T)$ in Figure 7 can be divided into two regions: (i) a linear region at low frequencies, corresponding to static conductivity σ_{DC} independent of frequency but dependent on temperature; and (ii) a dispersion region at high frequencies, corresponding to the dynamic conductivity σ_{AC} dependent on both frequency and temperature. From Figure 7a, it can be observed that, in the case of sample A (manganese ferrite MnFe_2O_4), the static conductivity σ_{DC} increases with temperature over the entire temperature range. In the case of sample B (manganese ferrite doped with Zn ions), the static conductivity σ_{DC} increases only at the beginning of the temperature range between 32 and 70 °C, after which a decrease in σ_{DC} with temperature is observed between 76 and 128 °C (see Figure 7b).

Figure 8 shows the temperature dependence of the static conductivity $\sigma_{DC}(T)$ for the two investigated samples.

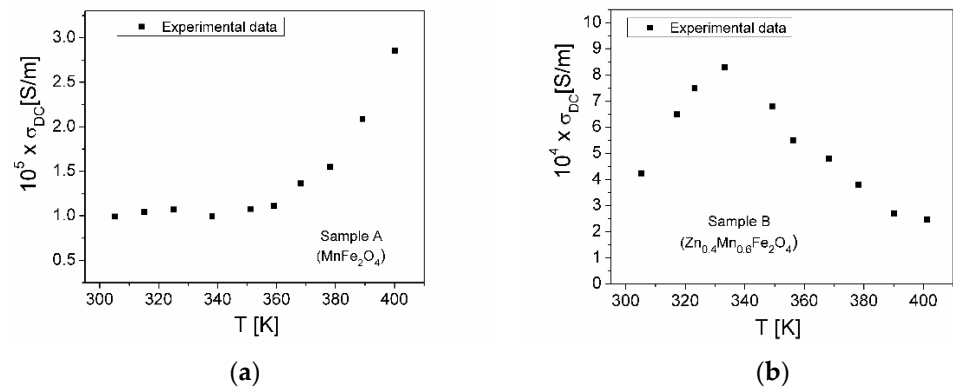


Figure 8. Temperature dependence of static conductivity σ_{DC} : (a) sample A (MnFe_2O_4); and (b) sample B ($\text{Zn}_{0.4}\text{Mn}_{0.6}\text{Fe}_2\text{O}_4$).

From Figure 8a, it can be seen that, in the case of sample A (MnFe_2O_4), the $\sigma_{DC}(T)$ component increases slightly when the temperature increases from 30 °C to approximately 70 °C, after which the increase is more pronounced at temperatures between 70 °C and 127 °C, indicating that the conduction process is thermally activated over the two temperature ranges, as in Ref. [13]. At the same time, the increase in conductivity σ_{DC} with temperature is due to the increase in the drift mobility of the charge carriers, according to Mott's VRH (variable range hopping) conduction mechanism [19].

In the case of sample B ($\text{Zn}_{0.4}\text{Mn}_{0.6}\text{Fe}_2\text{O}_4$), the conductivity $\sigma_{DC}(T)$ increases when the temperature increases from 30 °C to about 60 °C (Figure 8b) and then decreases with increasing temperatures from 60 °C to 128 °C. Thus, unlike the results published in Ref. [13], we highlighted that, around the temperature of 60 °C, there is a transition from a semiconductor behavior to a conductor behavior. In the low-temperature range, the electrons are not free, and the conductivity increases with increasing temperatures, with this behavior being a semiconductor-type behavior. At temperatures above 60 °C, the static conductivity decreases with increasing temperatures, the sample behaving like a conductor [19]. On the other hand, from Figure 8, it can be observed that, in the case of the Zn substitution of manganese ferrite (sample B), the conductivity σ_{DC} of the Mn-Zn ferrite increases by an order of magnitude compared to the static conductivity σ_{DC} of unsubstituted manganese ferrite MnFe_2O_4 .

Based on Mott's VRH model [19], the temperature dependence of the static conductivity σ_{DC} is described by the following equation:

$$\sigma_{DC} = \sigma_0 \exp\left(-\frac{D}{T^{1/4}}\right) \quad (5)$$

where D is given by the equation

$$D = \frac{4E_{cond}}{kT^{3/4}} \quad (6)$$

In these relationships, σ_0 is the pre-exponential factor, and E_{cond} is the activation energy for electrical conduction [19,42]. The experimental dependence of $\ln\sigma_{DC}$ on $T^{-1/4}$ of the samples, using Equation (5), is shown in Figure 9. The measurement error of $\ln\sigma_{DC}$ is approximately 1% and is represented in Figure 9a,b with error bars.

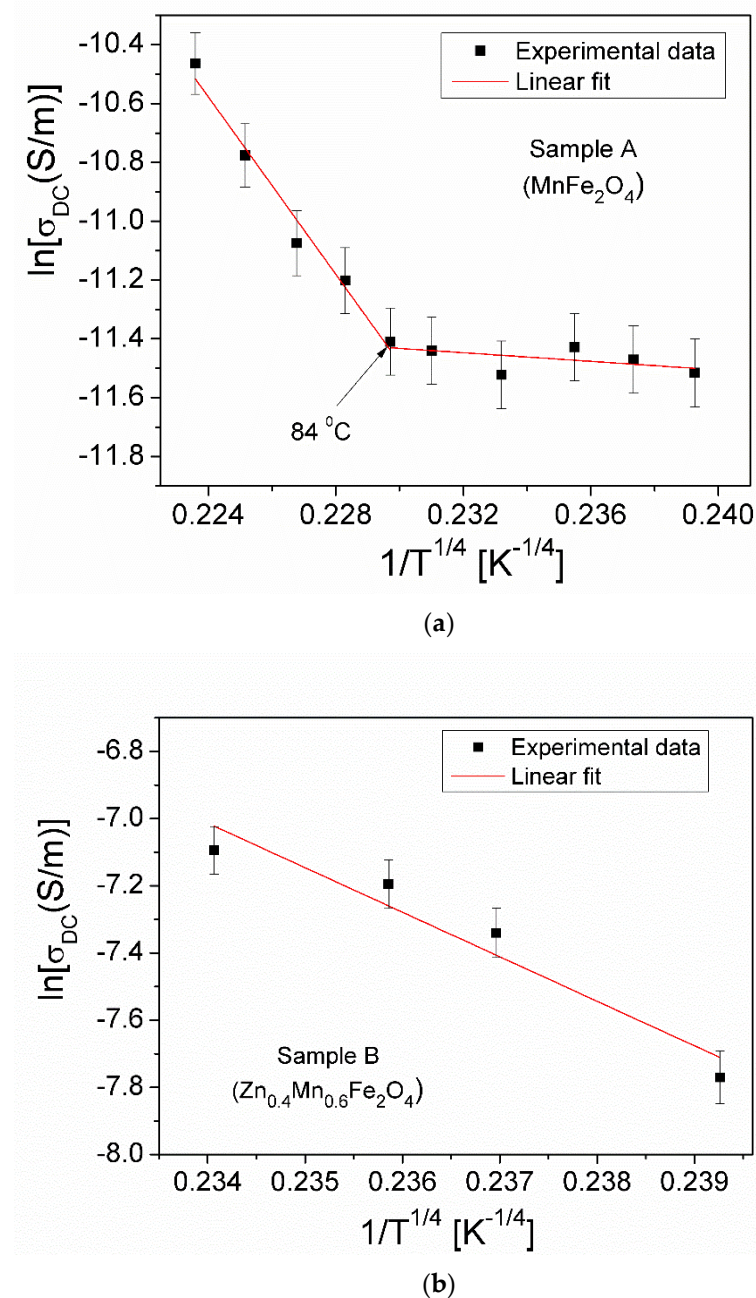


Figure 9. The dependence $\ln\sigma_{DC}(T^{-1/4})$ for (a) sample A (MnFe_2O_4) and (b) sample B ($\text{Zn}_{0.4}\text{Mn}_{0.6}\text{Fe}_2\text{O}_4$).

From Figure 9, one can observe that, for sample A of manganese ferrite, there is a change in the slope of the curve at a temperature of 84 °C; this fact is both due to the ferrite nanoparticles (*grains*) but also to the separation limits between the nanoparticles (*grain boundaries*) [40,42], which cause the sample conductivity to change. This result is in agreement with the one obtained in Figure 6a, in which the plot dependence $\ln(\tau)$ on

($1000/T$) changes its slope at a temperature of $85\text{ }^{\circ}\text{C}$, causing an increase in electrical conductivity (above $85\text{ }^{\circ}\text{C}$). Fitting the $\ln\sigma_{DC}(T^{-1/4})$ dependencies in Figure 9 with a straight line, both the slope D corresponding to the two temperature ranges (below $84\text{ }^{\circ}\text{C}$ and above $84\text{ }^{\circ}\text{C}$, respectively) for sample A (Figure 9a) and the slope D corresponding to the temperature range for sample B (Figure 9b) were determined. The following fitting parameters of sample A were obtained: for the temperature range below $84\text{ }^{\circ}\text{C}$, the intercept was -9.74876 , and slope D was -7.32114 , and, for the temperature range above $84\text{ }^{\circ}\text{C}$, the intercept was 23.20753 , and slope D was -150.82696 . In the case of sample B, the intercept was 24.01423 , and slope D was -132.59746 for the temperature range between 30 and $60\text{ }^{\circ}\text{C}$. Then, using Equation (6), we were able to calculate the activation energy for conduction $E_{cond}(T)$ for the two samples. Figure 10 shows the temperature dependence of the activation energy $E_{cond}(T)$ for samples A and B in the temperature ranges at which the conductivity variation occurs with the same slope.

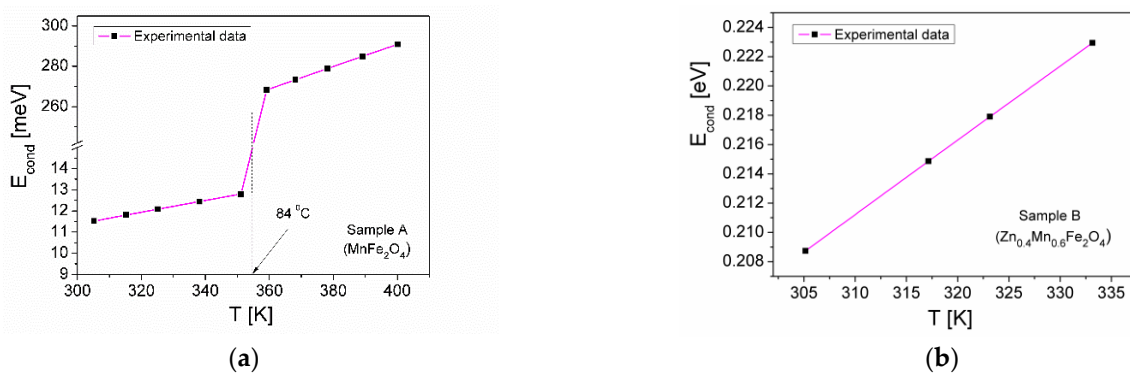


Figure 10. Temperature dependence of the activation energy for conduction E_{cond} in the case of sample A (a) and sample B (b).

From Figure 10, it turns out that the E_{cond} for both samples increases linearly with the increasing temperature, which indicates that the electrical conduction in the investigated samples can be explained by the process of hopping electrons between localized states, in accordance with the VRH model [19]. For sample A, the values obtained for E_{cond} in the temperature range $32\text{--}78\text{ }^{\circ}\text{C}$ are between 11 and 12.5 meV, and, in the temperature range $80\text{--}127\text{ }^{\circ}\text{C}$, they are between 0.260 and 0.295 eV (Figure 10a). For sample B (Figure 10b), the values obtained for E_{cond} in the temperature range $32\text{--}60\text{ }^{\circ}\text{C}$ are between 0.207 and 0.225 eV. These values of E_{cond} for the two samples are close to the values obtained from the electrical relaxation measurements for the barrier energy between the localized states of the samples, ΔE_{relax} , in the same temperature ranges, according to Figure 6a,b.

From the values obtained for ΔE_{relax} and E_{cond} , in the same temperature ranges, it can be noted that the ΔE_{relax} value is the average value of the interval corresponding to the activation energy of the conduction process, E_{cond} . As a result, it can be said that ΔE_{relax} represents the energy required for hopping between the localized states of the charge carriers.

In the dispersion region at high frequencies, the dynamic conductivity σ_{AC} is correlated with the relaxation processes determined by the electric localized charge carriers in the sample [41], given by the following relationship:

$$\sigma_{AC}(\omega, T) = A_0 \omega^{n(T)} = \sigma_{DC} \left(\frac{\omega}{\omega_c} \right)^{n(T)} \quad (7)$$

where A_0 is a temperature-dependent parameter; the exponent n is dimensionless, dependent on temperature ($n < 1$) [20,41]; and ω_c represents the crossover frequency, i.e., the transition frequency from the static regime, DC, to the dynamic regime, AC, of electrical

conductivity (see Figure 6), in accordance with Jonscher's law [41]. From Equation (7), the following equation is derived:

$$\omega_c = \left(\frac{\sigma_{DC}}{A_0} \right)^{1/n} \quad (8)$$

which allows the crossover frequency to be determined, based on electrical conductivity measurements and the VRH model. The experimental dependence $\ln(\sigma_{AC})$ on $\ln(\omega)$, obtained by the logarithm in Equation (7), at all the investigated temperatures, is shown in Figure 11, for both samples. The exponent n and parameter A_0 for each temperature of the two samples can be determined by fitting with the straight line of the experimental dependence, $\ln(\sigma_{AC})$ on $\ln(\omega)$, from Figure 11. For all the investigated temperatures T , the fitting parameters $\ln A_0$ and the exponents n and R^2 corresponding to each sample, obtained by fitting the experimental dependences from Figure 11a,b, are shown in Table 3.

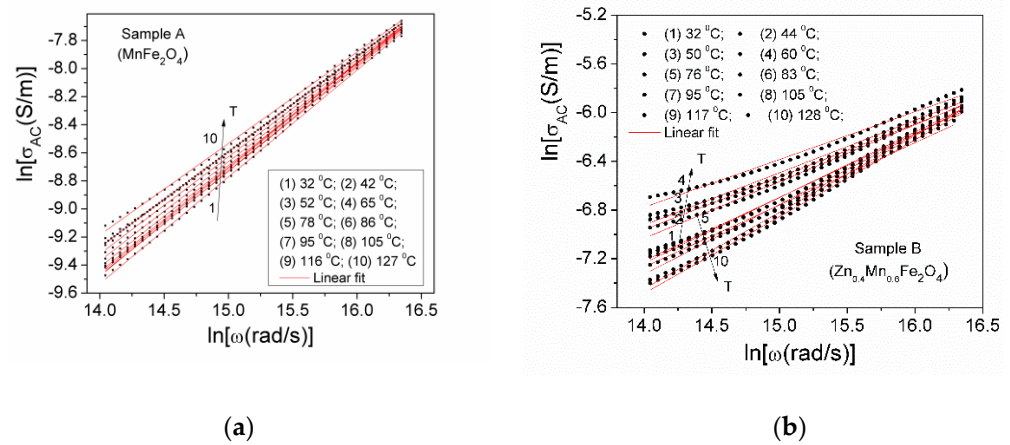


Figure 11. $\ln(\sigma_{AC})$ dependence on $\ln(\omega)$ at different temperatures for (a) sample A (MnFe_2O_4) and (b) sample B ($\text{Zn}_{0.4}\text{Mn}_{0.6}\text{Fe}_2\text{O}_4$).

Table 3. Values of the fitting parameters of the experimental dependencies $\ln(\sigma_{AC})$ on $\ln(\omega)$, from Figure 11, for the $\text{Zn}_x\text{Mn}_{1-x}\text{Fe}_2\text{O}_4$ ($x = 0$ and 0.4) ferrite samples.

Sample A				Sample B			
T_A (°C)	$\ln[A_0 \text{ (S/ms}^n\text{)}]$	n	R^2	T_B (°C)	$\ln[A_0 \text{ (S/ms}^n\text{)}]$	n	R^2
32	−19.97196	0.75	0.9995	32	−14.41251	0.510	0.9934
42	−19.87659	0.745	0.9994	44	−13.02810	0.433	0.9910
52	−19.97192	0.749	0.9995	50	−12.94721	0.430	0.9909
65	−20.17897	0.760	0.9995	60	−12.26714	0.392	0.9878
78	−19.86704	0.742	0.9995	76	−13.55826	0.466	0.9918
86	−19.55269	0.724	0.9995	83	−14.5103	0.521	0.9947
95	−19.27013	0.707	0.9994	95	−14.7734	0.538	0.9957
105	−19.00402	0.691	0.9993	105	−15.37215	0.574	0.9971
116	−18.77898	0.679	0.9992	117	−16.30916	0.630	0.99738
127	−18.29831	0.651	0.9989	128	−16.23992	0.628	0.9984

Figure 12 shows the temperature dependence of the exponent n for each ferrite sample. From Figure 12a, it can be seen that the exponent n for sample A (MnFe_2O_4) increases very slightly around the value of 0.75 when the temperature increases from 30 °C to 70 °C and then rapidly decreases to the value of 0.65 when the temperature increases from 70 °C to 127 °C. From Figure 12b, it can be observed that the exponent n for sample B ($\text{Zn}_{0.4}\text{Mn}_{0.6}\text{Fe}_2\text{O}_4$) decreases from 0.51 to 0.39 when the temperature increases from 30 °C to 60 °C, while, at temperatures above 60 °C, n increases from 0.39 to 0.63. At the same time, from Figure 12, it can be observed that the exponent n has relatively high values ($n > 0.5$),

which shows that, in the investigated samples, the conduction mechanism is due to a process of the charge carriers from the material hopping between the closer neighboring states, according to the CBH (correlated barrier hopping) model [43]. According to this model, the exponent n can be written in a first approximation [20,43] in the following form:

$$n = 1 - \frac{6kT}{W_m} \quad (9)$$

where W_m represents the maximum energy of the barrier, considered equal to the energy of the bandgap [43]. Knowing the obtained values of n , shown in Figure 12, for the investigated samples, using Equation (9), the energy of the bandgap W_m was determined, at all the investigated temperatures, with the obtained results also being shown in Figure 12.

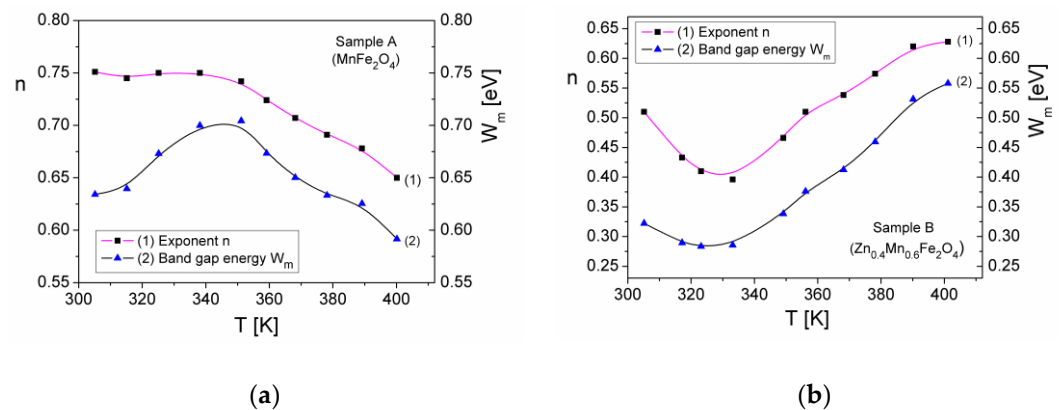


Figure 12. Temperature dependence of the exponent n and the bandgap energy W_m for (a) sample A (MnFe₂O₄) and (b) sample B (Zn_{0.4}Mn_{0.6}Fe₂O₄).

As seen in Figure 12a,b, by adding metal ions of Zn in the MnFe₂O₄ spinel ferrite structure, there is a decrease in the energy of the bandgap (Figure 12b), compared to the unsubstituted MnFe₂O₄ ferrite (Figure 12a). At the same time, from Figure 12, it can be seen that, in the case of manganese ferrite (sample A), W_m has a maximum equal to 0.72 eV at a temperature of 70–80 °C, while, for the Mn-Zn ferrite sample (sample B), W_m has a minimum equal to 0.28 eV at a temperature of 60 °C. The maximum value of the bandgap energy W_m for sample A correlates very well with the static conductivity σ_{DC} , which has a minimum at the respective temperatures for sample A (see Figure 8a). Similarly, the minimum value of the bandgap energy W_m for sample B correlates very well with the static conductivity σ_{DC} , which has a maximum at the temperature of 60 °C (see Figure 8b). The values obtained by us for the bandgap energy W_m in Figure 12 are consistent with those obtained by other authors [44,45] for samples of manganese ferrite MnFe₂O₄ or manganese ferrite substituted with Cu²⁺ or Ca ions (values between 1 eV and 2 eV).

Knowing the values of the parameters n and A_0 determined by fitting the straight line of the experimental dependence $\ln(\sigma_{AC})$ of $\ln(\omega)$ from Figure 11, as well as the σ_{DC} values of the electrical conductivity (Figure 8), for each temperature of the two samples, with Equation (8), we calculated the values of the crossover frequency ω_c . Figure 13 shows the temperature dependence of the frequency $f_c = \omega_c/2\pi$ for the two samples.

From Figure 13a, it can be seen that, in the case of sample A (MnFe₂O₄), the transition frequency f_c , from the DC regime to the AC regime, increases slightly from 12.5 kHz to 14 kHz when the temperature increases from 30 °C to approximately 70 °C, after which the increase is more pronounced, up to 27 kHz, at temperatures between 70 °C and 127 °C. At the same time, in the case of Mn-Zn ferrite (sample B, Zn_{0.4}Mn_{0.6}Fe₂O₄), the f_c frequency increases from 71 kHz to 109 kHz when the temperature increases from 30 °C to about 60 °C (Figure 13b) and then decreases to the value of 45 kHz with increasing temperatures from 60 °C to 128 °C. This behavior of the transition frequencies f_c of samples A and B is

similar to the experimental temperature dependence of the DC conductivity (see Figure 6), which is in agreement with the VRH theory of Mott and Davis [19].

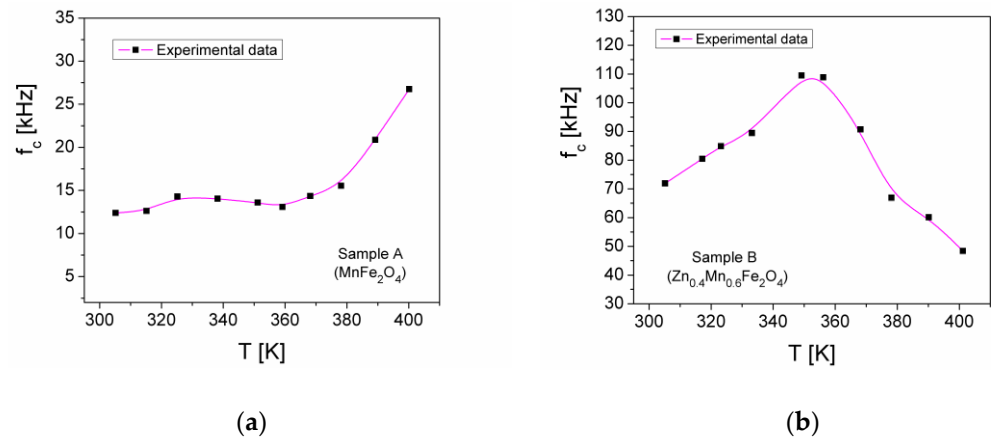


Figure 13. Temperature dependence of the crossover frequency $f_c = \omega_c/2\pi$: (a) sample A (MnFe_2O_4); and (b) sample B ($\text{Zn}_{0.4}\text{Mn}_{0.6}\text{Fe}_2\text{O}_4$).

3.5.3. Complex Dielectric Permittivity

In recent years, studies have been carried out on the electrical properties in the high-frequency range (tens of kHz to hundreds of MHz) of some artificial composite materials, such as ceramic materials doped with indium [46] or cermet-type materials doped with copper [47]. For these materials, authors have highlighted a negative dielectric permittivity, as they have a behavior like that of a metamaterial [48], being able to be used in applications with coil-less electrical inductors and electromagnetic shielding. At the same time, a great technological interest for researchers relates to the study of the electrical properties in the microwave field of some materials resulting from the combination of hexaferrite with spinel ferrite (AFe_2O_4 , where $A = \text{Co}, \text{Ni}, \text{Cu}, \text{Zn},$ and Mn) [49]. This results in a new functional material characterized by magneto-dielectric and absorption properties in the microwave range.

To determine the real (ϵ') and imaginary (ϵ'') components of complex dielectric permittivity in the $\text{Zn}_x\text{Mn}_{1-x}\text{Fe}_2\text{O}_4$ ferrite samples ($x = 0$ and 0.4), based on complex impedance measurements in the low-frequency field, we used the following equations:

$$\epsilon' = \frac{1}{\omega\epsilon_0} \frac{Z''}{Z'^2 + Z''^2} \frac{d}{A} \quad (10)$$

$$\epsilon'' = \frac{1}{\omega\epsilon_0} \frac{Z'}{Z'^2 + Z''^2} \frac{d}{A} \quad (11)$$

where ϵ_0 is the dielectric permittivity of free space ($\epsilon_0 = 8.856 \cdot 10^{-12}$ F/m).

Figure 14 shows the frequency dependence of the real ϵ' and imaginary ϵ'' components of complex dielectric permittivity at different temperatures for the two investigated samples.

From Figure 14a,c, we can see that the values of the real component ϵ' at the frequency of 100 Hz are between 300 and 800. For sample A, the ϵ' value increases by increasing the temperature over the entire temperature range (Figure 14a). In the case of sample B, the increase in ϵ' is observed in the range of 32–60 °C, after which ϵ' decreases as the temperature increases up to 128 °C (Figure 14c). This behavior of ϵ' can be correlated with the conduction mechanism in ferrites and is explained by the hopping between Fe^{2+} and Fe^{3+} ions on octahedral sites [40,50]. Also, in Mn-Zn ferrite (sample B) in tetrahedral sites due to the volatility of the Zn^{2+} ion, by increasing the temperature, part of the Fe^{2+} ions from the octahedral sites will be forced to transfer to the tetrahedral sites, which will lead to an increase in dielectric permeability [40,50]. By increasing the frequency, the ϵ' component

of the dielectric permittivity decreases significantly at high frequencies (over 200 kHz), tending towards the value of approximately 100 (Figure 14a,c), which shows that the charge carriers are influenced by the interfacial polarization mechanism [51].

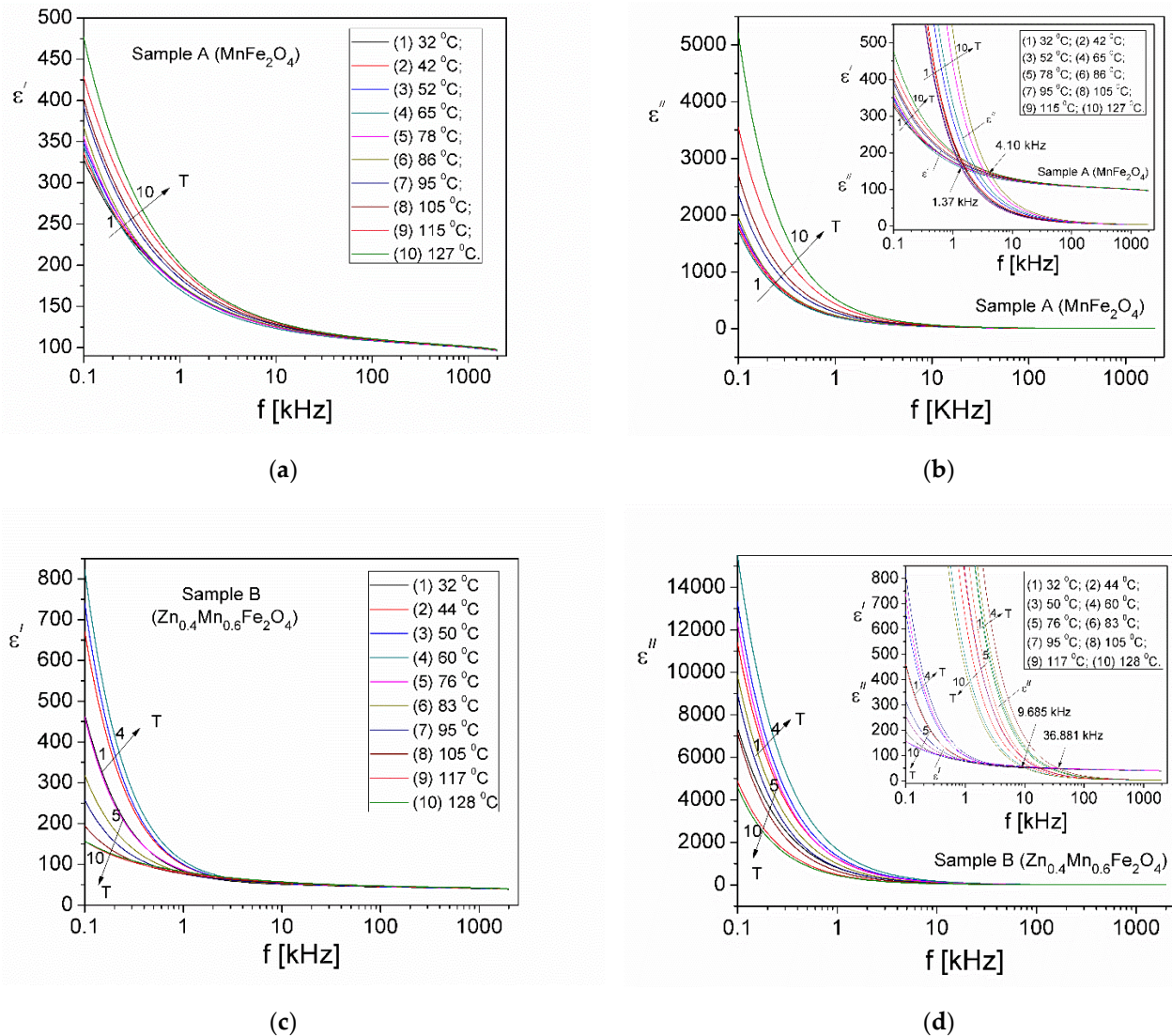


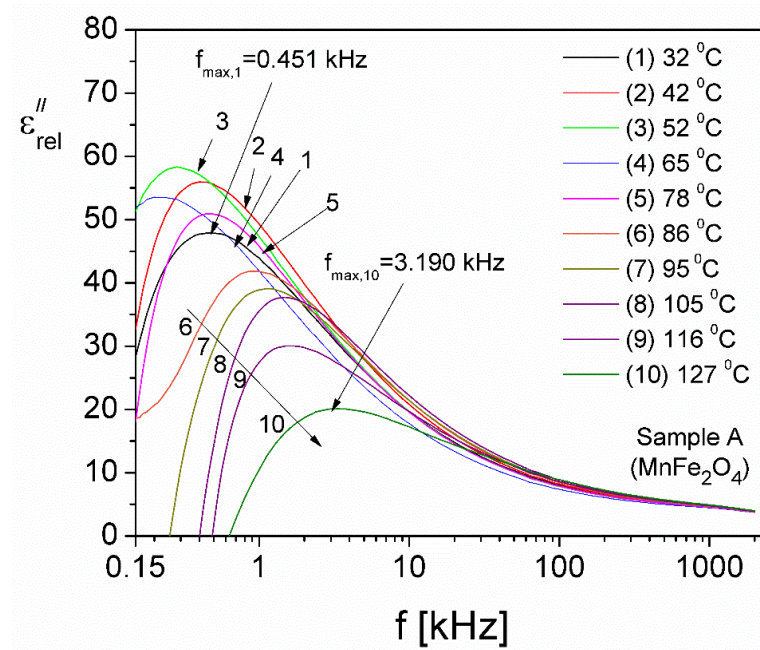
Figure 14. Temperature dependence of the real ϵ' and imaginary ϵ'' components of complex dielectric permittivity at different temperatures for (a,b) sample A of MnFe_2O_4 and (c,d) sample B of $\text{Zn}_{0.4}\text{Mn}_{0.6}\text{Fe}_2\text{O}_4$.

From Figure 14b,d, it can be observed that the values of the imaginary component ϵ'' for both samples, at low frequencies, are between 1700 and 15,000 and decrease rapidly by increasing the frequency, for any temperature value. At the same time, it can be observed that the values of ϵ'' are much higher than the values of the component ϵ' for all temperatures T (see inset in Figure 14b,d), up to the frequencies included in the range of 1.37–4.10 kHz (sample A) and, respectively, 9.685–36.881 kHz (sample B). This shows us that, up to these frequencies, there are large conduction losses in the inherited samples. Over the frequencies between approximately 1.37 and 4.10 kHz (sample A) and, respectively, between 9.685 and 36.881 kHz (sample B), corresponding to all the T values of the temperature (see Figure 14b,d), the values of ϵ'' decrease below the values of ϵ' , thus indicating that conduction losses become negligible and dielectric relaxation losses become important. It is known that the total dielectric losses in a material [52] are determined by

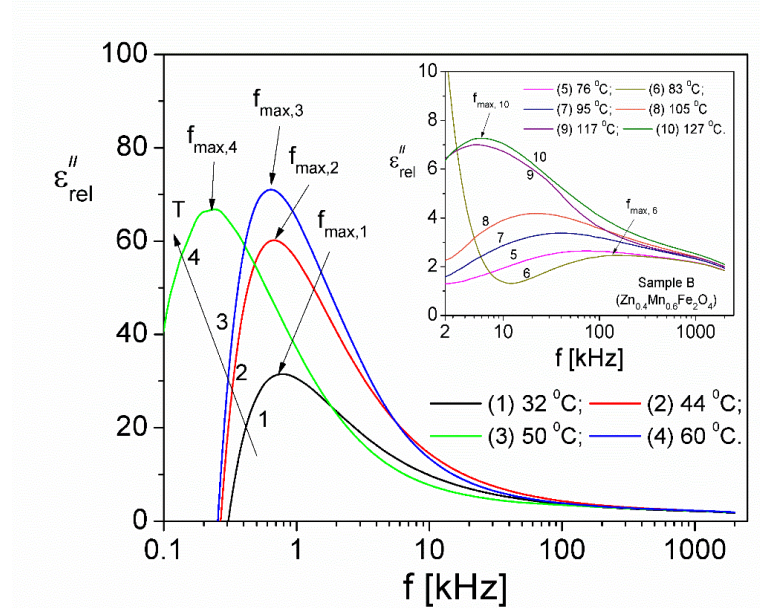
both electrical conduction (conduction losses, ϵ''_{cond}) and dielectric relaxation (relaxation losses, ϵ''_{rel}). As a result,

$$\epsilon''(\omega) = \epsilon''_{rel}(\omega) + \epsilon''_{cond}(\omega) \tag{12}$$

Taking into account that $\epsilon''_{cond} = \sigma / \omega \epsilon_0$ [52] and assuming $\sigma = \sigma_{DC}$, corresponding to each temperature T (see Figure 8), with Equation (12), we were able to determine the component ϵ''_{rel} , due only to the dielectric relaxation of the investigated samples. The frequency dependence of the component ϵ''_{rel} at different temperatures is presented in Figure 15.



(a)



(b)

Figure 15. Frequency dependence of the imaginary component ϵ''_{rel} , due to dielectric relaxation, at different temperatures for (a) sample A and (b) sample B.

From Figure 15, it can be seen that ϵ''_{rel} has a maximum at f_{max} frequency, corresponding to each temperature T , which indicates the existence of a relaxation process attributed to interfacial relaxation [53]. Using the experimental values of f_{max} from Figure 15a,b and the Debye equation, the relaxation times due to the interfacial relaxation process τ_{rel} for each investigated sample were determined. The temperature dependence of τ_{rel} for samples A and B is shown in Figure 16.

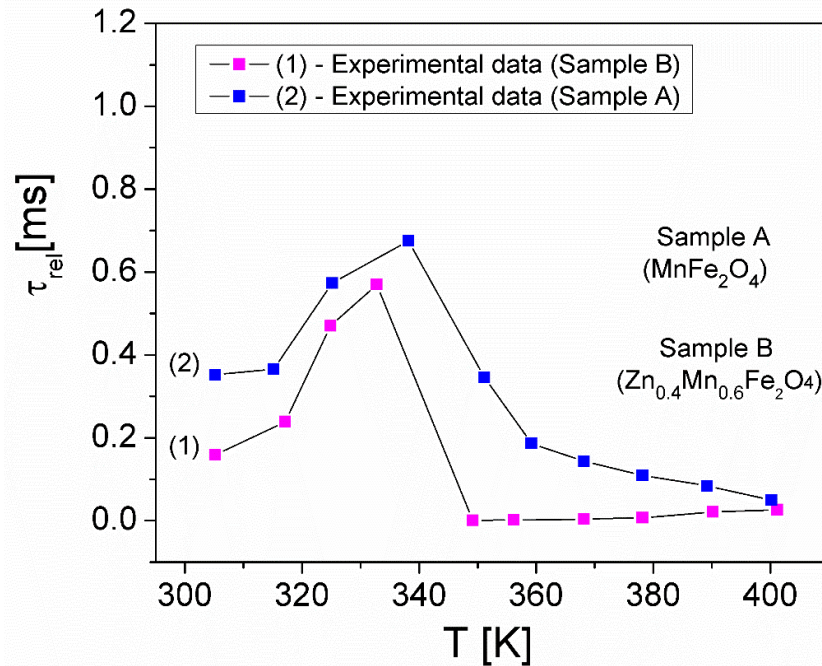


Figure 16. Temperature dependence of the relaxation time τ_{rel} due to the dielectric relaxation process.

As seen from Figure 16, for manganese ferrite (sample A), τ_{rel} increases in the temperature range of 32–65 °C, after which it decreases when the temperature increases from 65 °C to 127 °C. In the case of Mn-Zn ferrite (sample B), the increase in τ_{rel} with temperature occurs both in the range of 30–60 °C and between 76 and 128 °C. This variation with temperature in the relaxation time τ_{rel} obeys an Arrhenius-type law, in the form of Equation (3), where we denoted with $E_{A,rel}$ the activation energy of the dielectric relaxation process for the two ferrite samples in different temperature ranges. Using Equation (3), by fitting the experimental dependence $(\ln\tau_{rel})(1/T)$ with a straight line, it is possible to determine the activation energy $E_{A,rel}$ corresponding to the mentioned temperature ranges for the two samples. The obtained values are the following: $E_{A,rel} = 0.195$ eV for sample A in the temperature range of 32–65 °C; $E_{A1,rel} = 0.430$ eV for sample B in the first temperature range (30–60 °C); and $E_{A2,rel} = 0.770$ eV for sample B in the second temperature range (76–128 °C). Similar values for the dielectric relaxation activation energy have been reported by other authors [40,42] for similar ferrite samples.

4. Conclusions

MnFe_2O_4 and $\text{Zn}_{0.4}\text{Mn}_{0.6}\text{Fe}_2\text{O}_4$ ferrite samples were prepared by the hydrothermal method. The X-ray diffractogram showed that the samples were well crystallized, without secondary phases and crystallized in the cubic spinel system with the Fd-3m space group, also confirmed by the FTIR absorption spectra of the samples. The magnetic measurements showed that, by doping manganese ferrite with Zn^{2+} ions, sample B of Mn-Zn ferrite had a superparamagnetic behavior, with a saturation magnetization σ_s lower than that of sample A of manganese ferrite. From the complex impedance measurements, over the frequency range 100 Hz–2 MHz and at different temperatures, between 30 and 130 °C, a maximum of the imaginary component Z'' of the complex impedance was highlighted at all the

investigated temperatures, which indicated the existence of an electrical relaxation process determined by the hopping of the charge carriers between localized states, in both samples. These measurements allowed the determination, for the first time, of the barrier energy between the localized states ΔE_{relax} of the samples, obtaining, for sample A, two values (0.012 eV and 0.283 eV) associated with two areas of different conductivities and, for sample B, a value equal to 0.221 eV. The frequency and temperature dependencies of both the electrical conductivity (σ) and the complex dielectric permittivity (ϵ) of the samples were determined, using the complex impedance measurements. The results show that, at all the investigated temperatures, the conductivity spectrum $\sigma(f)$ for the two investigated samples consisted of both the static component σ_{DC} , corresponding to low frequencies, and the dynamic component σ_{AC} , which increased rapidly with frequency and corresponded to high frequencies, in agreement with Jonscher's law. The σ_{DC} component for sample B ($Zn_{0.4}Mn_{0.6}Fe_2O_4$ ferrite) was an order of magnitude higher than the σ_{DC} conductivity of sample A (manganese ferrite, $MnFe_2O_4$). Based on the temperature dependence of the static conductivity $\sigma_{DC}(T)$ and Mott's VRH model, the temperature dependence of the activation energy of the conduction process $E_{cond}(T)$ in the investigated samples was determined. The results show that the values of E_{cond} for the two samples were close to the values obtained for the barrier energy between the localized states ΔE_{relax} of the samples in the same temperature ranges. As a result, it can be stated that ΔE_{relax} represented the energy required for the hopping of the charge carriers between the localized states, thus ensuring electrical conduction in the samples. In the dispersion region, at frequencies over to 200 kHz, using the CBH theoretical model, the temperature dependence of the bandgap energy (W_m) of both of the samples was determined for the first time. The obtained results show that, by adding Zn^{2+} ions to the manganese spinel ferrite structure, there was a decrease in the bandgap energy W_m , compared to the W_m of unsubstituted $MnFe_2O_4$ ferrite, from a maximum $W_m = 0.72$ eV (sample A) at a minimum $W_m = 0.28$ eV (sample B), in the temperature range of 60–70 °C. At the same time, based on the VRH and CBH models, we determined, for the first time, both for manganese ferrite (sample A) and Mn-Zn ferrite (sample B), the transition frequency f_c from the DC regime to the AC regime at all the investigated temperatures. The results obtained for the complex dielectric permittivity of the samples show that, after the elimination of the conduction losses, the imaginary component (ϵ'') due to the dielectric relaxation showed a maximum at the frequency f_{max} , which changed with temperature, proving the existence of a relaxation process attributed to the interfacial relaxation. The activation energy of the dielectric relaxation process $E_{A,rel}$ was determined for the two ferrite samples in different temperature ranges.

Author Contributions: Conceptualization, I.M. and C.N.M.; methodology, M.O.B.; software, C.N.M. and P.S.; validation, I.M., C.N.M. and M.O.B.; formal analysis, P.V.; investigation, I.M., P.S., and P.V.; resources, C.N.M. and M.O.B.; writing—original draft preparation, I.M.; writing—review and editing, C.N.M. and I.M.; visualization, M.O.B., P.S. and P.V.; supervision, I.M. and C.N.M. All authors have read and agreed to the published version of the manuscript.

Funding: This research received no external funding.

Data Availability Statement: The raw data supporting the conclusions of this article will be made available by the authors on request.

Acknowledgments: Paula Sfirloaga acknowledges partial support for the SEM-EDX measurements, in the frame of POC/1025/1/3, Cod SMIS 2014+ 156350.

Conflicts of Interest: The authors declare no conflicts of interest.

References

1. Kefeni, K.K.; Msagati, T.A.; Mamba, B.B. Ferrite nanoparticles: Synthesis, characterization and applications in electronic device. *Mater. Sci. Eng. B* **2017**, *215*, 37–55. [[CrossRef](#)]
2. Tsakaloudi, V.; Zaspalis, V.T. A new Mn–Zn ferrite for high-speed data transmission applications in telecommunication networks. *J. Magn. Magn. Mater.* **2007**, *310*, 2540–2542. [[CrossRef](#)]

3. Sahoo, B.; Devi, K.S.P.; Dutta, S.; Maiti, T.K.; Pramanik, P.; Dhara, D. Biocompatible mesoporous silica-coated superparamagnetic manganese ferrite nanoparticles for targeted drug delivery and MR imaging applications. *J. Colloid Interf. Sci.* **2014**, *431*, 31–41. [[CrossRef](#)] [[PubMed](#)]
4. Desai, H.B.; Hathiya, L.J.; Joshi, H.H.; Tanna, A.R. Synthesis and Characterization of Photocatalytic MnFe₂O₄ Nanoparticles. *Mat. Today Proc.* **2020**, *21*, 1905–1910. [[CrossRef](#)]
5. Arulmurugan, R.; Vaidyanathan, G.; Sendhilnathan, S.; Jeyadevan, B. Mn–Zn ferrite nanoparticles for ferrofluid preparation: Study on thermal–magnetic properties. *J. Magn. Magn. Mater.* **2006**, *298*, 83–94. [[CrossRef](#)]
6. Kamar, E.M.; Khairy, M.; Mousa, M.A. Effect of morphology and particle size on the electrical properties of nano-nickel ferrite. *J. Mat. Res. Technol.* **2023**, *24*, 7381–7393. [[CrossRef](#)]
7. Kardile, H.; Somvanshi, S.B.; Chavan, A.R.; Pandit, A.; Jadhav, K. Effect of Cd²⁺ doping on structural, morphological, optical, magnetic and wettability properties of nickel ferrite thin films. *Optik* **2020**, *207*, 164462. [[CrossRef](#)]
8. Kaur, N.; Kaur, M. Comparative studies on impact of synthesis methods on structural and magnetic properties of magnesium ferrite nanoparticles. *Process. Appl. Ceram.* **2014**, *8*, 137–143. [[CrossRef](#)]
9. Malaescu, I.; Lungu, A.; Marin, C.N.; Vlazan, P.; Sfirloaga, P.; Turi, G.M. Experimental investigations of the structural transformations induced by the heat treatment in manganese ferrite synthesized by ultrasonic assisted co-precipitation method. *Cer. Int.* **2016**, *42*, 16744–16748. [[CrossRef](#)]
10. Humbe, A.V.; Kounsalye, J.S.; Somvanshi, S.B.; Kumar, A.; Jadhav, K. Cation distribution, magnetic and hyperfine interaction studies of Ni–Zn spinel ferrites: Role of Jahn Teller ion (Cu²⁺) substitution. *Mater. Adv.* **2020**, *1*, 880–890. [[CrossRef](#)]
11. Anupama, M.; Srinatha, N.; Matteppanavar, S.; Angadi, B.; Sahoo, B.; Rudraswamy, B. Effect of Zn substitution on the structural and magnetic properties of nanocrystalline NiFe₂O₄ ferrites. *Ceram. Int.* **2018**, *44*, 4946–4954. [[CrossRef](#)]
12. Kumar, D.R.; Lincoln, C.A.; Ravinder, D.; Ahmad, S.I. Structural, morphological, luminescence, magnetic, and electrical transport properties of zinc-doped MnFe₂O₄ nanomaterials. *Appl. Phys. A* **2020**, *126*, 705. [[CrossRef](#)]
13. Rafique, T.; Atif, M.; Rehman, A.U.; Wahab, H.; Khalid, W.; Ali, Z.; Nadeem, M. Colossal permittivity, resistive and magnetic properties of zinc substituted manganese ferrites. *J. Alloys Comp.* **2022**, *923*, 166454. [[CrossRef](#)]
14. Gimenes, R.; Baldissera, M.R.; Da Silva, M.R.A.; Da Silveira, C.A.; Soares, D.A.W.; Perazolli, P.A.; Da Silva, M.R.; Zaghete, M.A. Structural and magnetic characterization of Mn_xZn_{1-x}Fe₂O₄ (x = 0.2, 0.35, 0.65, 0.8, 1.0) ferrites obtained by the citrate precursor method. *Ceram. Int.* **2012**, *38*, 741–746. [[CrossRef](#)]
15. Makovec, D.; Drogenik, M.; Žnidaršič, A. Sintering of MnZn-ferrite powders prepared by hydrothermal reactions between oxides. *J. Eur. Ceram. Soc.* **2001**, *21*, 1945–1949. [[CrossRef](#)]
16. Gopalan, E.V.; Al-Omari, I.A.; Malini, K.A.; Joy, P.A.; Kumar, D.S.; Yoshida, Y. Impact of zinc substitution on the structural and magnetic properties of chemically derived nanosized manganese zinc mixed ferrites. *J. Magn. Magn. Mater.* **2009**, *321*, 1092–1099. [[CrossRef](#)]
17. El Heda, I.; Dhahri, R.; Massoudi, J.; Dhahri, E.; Bahri, F.; Khirouni, K.; Costa, B.F.O. Study of the structural, electrical, dielectric properties and transport mechanisms of Cu_{0.5}Fe_{2.5}O₄ ferrite nanoparticles for energy storage, photocatalytic and microelectronic applications. *Heliyon* **2023**, *9*, e17403. [[CrossRef](#)]
18. Coulibaly, S.; Malec, D.; Bley, V.; Mary, D.; Schlegel, B. New Use of Mn-Zn Ferrite Material in Power Electronics Integrated LC Filters. *Engineering* **2017**, *9*, 993–1007. [[CrossRef](#)]
19. Mott, N.F.; Davis, E.A. *Electronic Processes in Non-Crystalline Materials*; Clarendon: Oxford, UK, 1979.
20. Elliot, S.R. A.c. conduction in amorphous chalcogenide and pnictide semiconductors. *Adv. Phys.* **1987**, *36*, 135–217. [[CrossRef](#)]
21. Kumar, P.; Pathak, S.; Jain, K.; Singh, A.; Basheed, G.A.; Pant, R.P. Low-temperature large-scale hydrothermal synthesis of optically active PEG-200 capped single domain MnFe₂O₄ nanoparticles. *J. Alloys Comp.* **2022**, *904*, 163992. [[CrossRef](#)]
22. Griffiths, P.; de Hasseth, J.A. *Fourier Transform Infrared Spectrometry*, 2nd ed.; Wiley-Blackwell Inc.: Hoboken, NJ, USA, 2007.
23. Ercuta, A. Sensitive AC hysteresigraph of extended driving field capability. *IEEE Trans. Instrum. Meas.* **2020**, *69*, 1643–1651. [[CrossRef](#)]
24. Lungu, A.; Malaescu, I.; Marin, C.N.; Vlazan, P.; Sfirloaga, P. The electrical properties of manganese ferrite powders prepared by two different methods. *Phys. B Cond. Matter.* **2015**, *462*, 80–85. [[CrossRef](#)]
25. *ASTM D150-98*; Standard Test Methods for AC Loss Characteristics and Permittivity (Dielectric Constant) of Solid Electrical Insulation. ASTM International: West Conshohocken, PA, USA, 2017.
26. Iyer, R.; Desai, R.; Upadhyay, R.V. Low temperature synthesis of nanosized Mn_{1-x}Zn_xFe₂O₄ ferrites and their characterizations. *Bull. Mater. Sci.* **2009**, *32*, 141–147. [[CrossRef](#)]
27. Srinivasan, T.T.; Srivastava, C.M.; Venkataramani, N.; Patni, M.J. Infrared absorption in spinel ferrites. *Bull. Mater. Sci.* **1984**, *6*, 1063–1067. [[CrossRef](#)]
28. Raju, M.K. FT-IR studies of Cu substituted Ni-Zn ferrites for structural and vibrational investigations. *Chem. Sci. Trans.* **2015**, *4*, 137–142.
29. Devi, E.C.; Soibam, I. Effect of Zn doping on the structural, electrical and magnetic properties of MnFe₂O₄ nanoparticles. *Indian J. Phys.* **2017**, *91*, 861–867. [[CrossRef](#)]
30. Liu, X.M.; Shao-Yun, F. Synthesis of nanocrystalline Zn_{0.5}Mn_{0.5}Fe₂O₄ via in situ polymerization technique. *J. Magn. Magn. Mater.* **2007**, *308*, 61–64. [[CrossRef](#)]

31. Zaag, P.J.V.; Noordermeer, A.; Johnson, M.T.; Bongers, P.E. Size-dependent Curie temperature in nanoscale MnFe_2O_4 particles. *Phys. Rev. Lett.* **1992**, *68*, 3112–3117. [[CrossRef](#)] [[PubMed](#)]
32. Gopalan, E.V.; Malini, K.A.; Saravanan, S.; Kumar, D.S.; Yoshida, Y.; Anantharaman, M.R. Evidence for polaron conduction in nanostructured manganese ferrite. *J. Phys. D Appl. Phys.* **2008**, *41*, 185005. [[CrossRef](#)]
33. Chen, J.P.; Sorenson, C.M.; Klabunde, K.J.; Hadjipanayis, G.G.; Delvin, E.; Kostidas, A. Size-dependent magnetic properties of MnFe_2O_4 fine particles synthesized by coprecipitation. *Phys. Rev. B* **1996**, *54*, 9288–9296. [[CrossRef](#)]
34. Arulmurugan, R.; Jeyadevan, B.; Vaidyanathan, G.; Sendhilnathan, S. Effect of zinc substitution on Co-Zn and Mn-Zn ferrite nanoparticles prepared by co-precipitation. *J. Magn. Magn. Mater.* **2005**, *288*, 470–477. [[CrossRef](#)]
35. Borsa, F.; Torgeson, D.R.; Martin, S.W.; Patel, H.K. Relaxation and fluctuations in glassy-fast-ion conductors Wide-frequency-range NMR and conductivity measurements. *Phys. Rev. B* **1992**, *46*, 795–801. [[CrossRef](#)]
36. Hajlaoui, M.E.; Dhahri, R.; Hnainia, N.; Benchaabane, A.; Dhahri, E.; Khirouni, K. Dielectric spectroscopy study of the $\text{Ni}_{0.2}\text{Zn}_{0.8}\text{Fe}_2\text{O}_4$ spinel ferrite as a function of frequency and temperature. *Mat. Sci. Eng. B* **2020**, *262*, 114683. [[CrossRef](#)]
37. Idrees, M.; Nadeem, M.; Hassan, M.M. Investigation of conduction and relaxation phenomena in $\text{LaFe}_{0.9}\text{Ni}_{0.1}\text{O}_3$ by impedance spectroscopy. *J. Phys. D Appl. Phys.* **2010**, *43*, 155401. [[CrossRef](#)]
38. Debye, P. *Polar Molecules*; Chemical Catalog Company, Inc.: New York, NY, USA, 1929.
39. Malaescu, I.; Lungu, A.; Marin, C.N.; Sfirloaga, P.; Vlazan, P.; Brindusoiu, S.; Poienar, M. Temperature dependence of the dynamic electrical properties of $\text{Cu}_{1+x}\text{Mn}_{1-x}\text{O}_2$ ($x = 0$ and 0.06) crednerite materials. *Cer. Intern.* **2018**, *44*, 11610–11616. [[CrossRef](#)]
40. Hajlaoui, M.E.; Gharbi, S.; Dhahri, E.; Khirouni, K. Impedance spectroscopy and giant permittivity study of spinel ZnFe_2O_4 ferrite as a function of frequency and temperature. *J. Alloys Comp.* **2022**, *906*, 164361. [[CrossRef](#)]
41. Jonscher, A.K. *Universal Relaxation Law*, 1st ed.; Chelsea Dielectrics Press: London, UK, 1996; pp. 198–200.
42. Ponpandian, N.; Balaya, P.; Narayanasamy, A. Electrical conductivity and dielectric behaviour of nanocrystalline NiFe_2O_4 spinel. *J. Phys. Condens. Matter.* **2002**, *14*, 3221–3237. [[CrossRef](#)]
43. Elliott, S.R. A theory of a.c. conduction in chalcogenide glasses. *Philos. Mag. B* **1977**, *36*, 1291–1304. [[CrossRef](#)]
44. Vijaya, J.; Sekaran, G.; Bououdina, M. Effect of Cu^{2+} doping on structural, morphological, optical and magnetic properties of MnFe_2O_4 particles/sheets/flakes-like nanostructures. *Ceram. Int.* **2015**, *41*, 15–26. [[CrossRef](#)]
45. Ustundağ, M.; Aslan, M. Electronic and Magnetic Properties of Ca-Doped Mn-Ferrite. *Acta Phys. Pol. A* **2016**, *130*, 362–364. [[CrossRef](#)]
46. Fan, G.; Wang, Z.; Sun, K.; Liu, Y.; Fan, R. Doped ceramics of indium oxides for negative permittivity materials in MHz-kHz frequency regions. *J. Mat. Sci. Technol.* **2021**, *61*, 125–131. [[CrossRef](#)]
47. Fan, G.; Wang, Z.; Ren, H.; Liu, Y.; Fan, R. Dielectric dispersion of copper/rutile cermet: Dielectric resonance, relaxation, and plasma oscillation. *Scripta Mater.* **2021**, *190*, 1–6. [[CrossRef](#)]
48. Xie, P.; Zhang, Z.; Liu, K.; Qian, L.; Dang, F.; Liu, Y.; Fan, R.; Wang, X.; Dou, S. C/SiO₂ meta-composite: Overcoming the λ/a relationship limitation in metamaterials. *Carbon* **2017**, *125*, 1–8. [[CrossRef](#)]
49. Trukhanov, A.V.; Algarou, N.A.; Slimani, Y.; Almessiere, M.A.; Baykal, A.; Tishkevich, D.I.; Vinnik, D.A.; Vakhitov, M.G.; Klygach, D.S.; Silibin, M.V.; et al. Peculiarities of the microwave properties of hard-soft functional composites $\text{SrTb}_{0.01}\text{Tm}_{0.01}\text{Fe}_{11.98}\text{O}_{19-A}\text{Fe}_2\text{O}_4$ ($A = \text{Co, Ni, Zn, Cu, or Mn}$). *RSC Adv.* **2020**, *10*, 32638–32651. [[CrossRef](#)] [[PubMed](#)]
50. Krishna, K.R.; Kumar, K.V.; Ravinder, D. Structural and Electrical Conductivity Studies in Nickel-Zinc Ferrite. *Adv. Mater. Phys. Chem.* **2012**, *02*, 185–191. [[CrossRef](#)]
51. Cao, M.S.; Song, W.L.; Hou, Z.L.; Wen, B.; Yuan, J. The effects of temperature and frequency on the dielectric properties, electromagnetic interference shielding and microwave-absorption of short carbon fiber/silica composites. *Carbon* **2010**, *48*, 788–796. [[CrossRef](#)]
52. Scaife, B.K. *Principles of Dielectrics*; Clarendon Press: Oxford, UK, 1998.
53. Batoo, K.M. Study of dielectric and impedance properties of Mn ferrites. *Phys. B Cond. Matter.* **2011**, *406*, 382–387. [[CrossRef](#)]

Disclaimer/Publisher’s Note: The statements, opinions and data contained in all publications are solely those of the individual author(s) and contributor(s) and not of MDPI and/or the editor(s). MDPI and/or the editor(s) disclaim responsibility for any injury to people or property resulting from any ideas, methods, instructions or products referred to in the content.